DOI: 10.13009/EUCASS2025-466
11TH EUROPEAN CONFERENCE FOR AERONAUTICS AND SPACE SCIENCES (EUCASS)

Advanced sensor tasking strategies for space objects cataloging

Alessandro Mignocchi[⋆,†], *Sebastian Samuele Rizzuto*[⋆], *Alessia De Riz*[⋆], *Marco Felice Montaruli*[⋆], *Pierluigi Di Lizia*[⋆], *Mauro Massari*[⋆]
[⋆]*Department of Aerospace Science and Technology, Politecnico Di Milano*
Via Giuseppe La Masa 32, Milan, 20156, Lombardy, Italy
alessandro.mignocchi@polimi.it · sebastiansamuele.rizzuto@polimi.it · alessia.deriz@polimi.it · marcofelice.montaruli@polimi.it · pierluigi.dilizia@polimi.it · mauro.massari@polimi.it
[†]Corresponding author

Abstract

Space Surveillance and Tracking (SST) is critical for maintaining an accurate catalog of space objects. This work presents the integrated development of observation strategies and a track-to-track correlation pipeline for space object cataloging within the SΞNSIT software. For HLEO targets, sensor tasking focuses on the Earth's shadow boundary to exploit optimal phase angles, while MEO-GEO regimes employ systematic equatorial-plane scans. Furthermore, the pipeline leverages Two-Body Integrals, uncertainty propagation, and a χ^2-test with the Squared Mahalanobis Distance to associate tracks. Results demonstrate that this integrated approach significantly enhances catalog build-up and overall SST performance.

1. Introduction

Space Surveillance and Tracking (SST) operations underpin the safe and sustainable utilization of Earth's orbits by providing continuous situational awareness of Resident Space Objects (RSOs)[5] . As the orbital environment becomes increasingly congested, the probability of conjunctions between operational spacecraft and fragments or between spacecraft themselves rises markedly, imposing substantial collision avoidance requirements on satellite operators. Moreover, uncontrolled re-entries of large debris pose non-negligible risks to terrestrial assets and populations, elevating the necessity for precise orbital monitoring and timely conjunction assessment[4] .

This complexity transcends any single orbital regime: Low Earth Orbit (LEO), Medium Earth Orbit (MEO), and Geostationary Orbit (GEO) all exhibit exponential growth in cataloged objects, driven by both intentional constellations and accidental fragmentation events. Ground- and space-based sensors collectively strive to maintain a comprehensive catalog, yet finite observational resources and competing priority tasks frequently result in coverage gaps[10] . Consequently, optimizing the end-to-end cataloging pipeline, from detection to orbit determination and update, becomes essential to maximize the utility of existing sensor networks and to ensure persistent surveillance.

To address these challenges, the sensor network simulation framework SΞNSIT[11] was upgraded within the context of this work, introducing an adaptive observation strategy for optical sensors that allows monitoring of both objects in low and high-altitude orbits. Across a single night campaign, this approach enables the detection, follow-up, and cataloging of heterogeneous orbital populations within a unified observation plan, thereby improving catalog update rates and reducing gaps in orbital coverage. Furthermore, to assess the performance in terms of object cataloging, the data generated by SΞNSIT are processed through its dedicated cataloging pipeline. This pipeline performs track-to-track association and enables the estimation of the target orbit using an Initial Orbit Determination (IOD) algorithm.

To isolate and highlight the performance of the new implementations, the scope of this study is deliberately limited to the track-to-track correlation stage. The recorded RSO detections are therefore passed only through the dedicated track-to-track association module of SΞNSIT. Extending the simulation to include full catalog build-up (i.e. complete track-to-track processing, IOD, and subsequent orbit updates for every object over the entire simulation window) would incur prohibitive computational costs. By stopping the analysis at the track-to-track level, this work can more clearly demonstrate the merits of the developed observation strategy-evaluated by the rate of detections[13]-and the track-to-track algorithm-evaluated by the rate of correct associations-without conflating these results with the downstream catalog maintenance process.

The newly developed algorithms were evaluated using specific populations of spacecraft in High LEO (HLEO), MEO,

Copyright © 2025 by PoliMi. Published by the EUCASS association with permission.

DOI: 10.13009/EUCASS2025-466

and GEO, as cataloged by the U.S. Space Surveillance Network (SSN). This assessment highlights the algorithms performance across diverse orbital regimes. Simulation results demonstrate the efficiency and accuracy of the proposed observational strategies and correlation algorithms within the SST framework.
The remainder of this paper is structured as follows. Section 2 presents the sensor network simulation software employed. Section 3 details the enhancements made to the software, including an in-depth description of the newly developed observation strategy (Subsection 3.1) and the track-to-track association and IOD algorithms (Subsection 3.2). Section 4 describes the simulation campaign used to evaluate these novel methodologies, and Section 5 offers concluding remarks, emphasizing the contributions of this work to space surveillance and tracking.

2. SΞNSIT

The Space Surveillance Sensor Network Simulation Tool (SΞNSIT)[11] is a robust software package developed by the Department of Aerospace Science and Technology (DAER) at Politecnico di Milano, with contributions from SpaceDyS. Written in `Python 3` and `C++`, SΞNSIT runs on Windows, macOS, and Linux, and leverages the NASA/NAIF SPICE library[2] for precise astronomical computations. Users may interact via a command-line interface or a Qt-based graphical user interface, with configuration managed through YAML files and internal data stored in an SQLite database.
SΞNSIT enables modeling complex sensor networks, both ground- and space-based, evaluating network performance in terms of coverage and catalog maintenance, and assessing sensitivity to configuration variations. Given a defined set of space objects, ground and space stations, and an observation time frame, the tool can compute the observation strategy and all observable transits, generate optimized observation schedules based on user criteria, simulate acquisitions and measurements, perform track-to-track and orbit determination with specified sensor accuracies, and incrementally build and maintain a catalog of tracked objects.
As illustrated in Figure 1, SΞNSIT is organized into six modules:

- **Data initialization:** pre-processes user inputs, updates SPICE kernels containing planetary ephemerides and leap-second data, and prepares the simulation environment.
- **Survey strategy definition:** computes the pointing sequence in terms of angles and time, following the observation strategy selected for each sensor.
- **Pass computation:** determines observable passes of objects under various geometrical and physical constraints.[3]
- **Observation scheduling:** uses a genetic algorithm to select and optimize subsets of computed passes on the sensor in tracking mode into efficient observation schedules.
- **Catalog build-up/maintenance:** simulates measurements from the schedule, performs orbit determination, and updates the network catalog iteratively.
- **Performance analysis:** analyzes module outputs via tables and charts, providing a comprehensive overview of network performance.

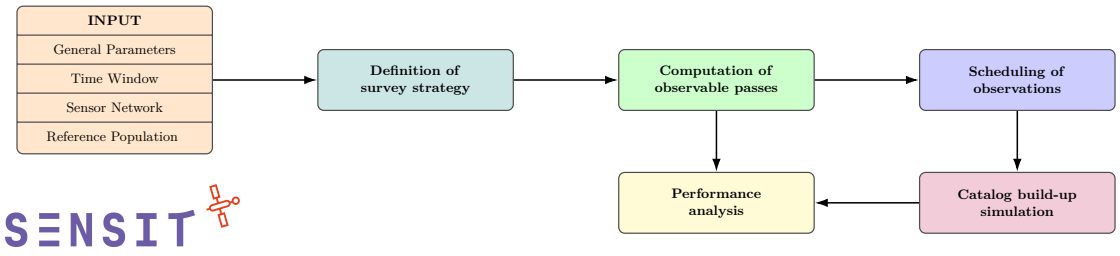

Figure 1: Block diagram of the SΞNSIT software architecture, showing the−end−to end pipeline from user-provided inputs (general parameters, time window, sensor network configuration, and reference population) through survey strategy definition, observable pass computation, observation scheduling, catalog build−up simulation, and concluding with performance analysis.

This study presents the newly developed implementation of SΞNSIT, with particular emphasis on the survey strategy module introduced herein, and the correlation pipeline, which plays a key role in catalog construction and maintenance, as detailed in Section 3.

DOI: 10.13009/EUCASS2025-466

3. Methodology and software upgrades

In this work, SΞNSIT has been extended to broaden its simulation capabilities, thus producing a more advanced and accurate tool for assessing both SST network performance and catalog fidelity. The survey strategy module was incorporated to enable the simulation of sensor pointing sequences instead of the fixed-point survey and tracking modes that characterized the previous software release. Furthermore, as detailed in Subsection 3.1, a novel observation strategy was developed and integrated to enhance optical sensors contribution and efficiency in monitoring large numbers of RSOs across multiple orbital regimes. Finally, Subsection 3.2 introduces a track-to-track pipeline within the catalog build-up and maintenance module, which further refines measurement processing.

3.1 Observation strategy

The observation strategy was tailored to maximize observational throughput over the course of a single night, thereby enabling the surveillance of a large population of RSOs across diverse orbital regimes with a particular focus on HLEO, MEO, and GEO. This composite methodology comprises two complementary scanning modes, each optimized to enhance both coverage and measurement fidelity:

- **Phase-aware fence:** this mode continuously scans the marginally illuminated boundary of Earth's shadow cone whenever it is visible. By targeting this specific region, the strategy optimizes the phase angle under which HLEO targets are observed, thereby improving Signal-to-Noise Ratio (SNR), reducing background contamination, and ultimately yielding higher-precision angular and photometric measurements of optical sensors.[6]
- **Equatorial fence:** operating in tandem with the phase-aware fence, this mode tracks the celestial band where RSOs intersect the Earth's equatorial plane. By persistently monitoring this region, the strategy ensures the detection of MEO and GEO populations, enhancing temporal revisit rates.

The phase-aware fence mode is activated only when the conical section of Earth's shadow, specified by a fixed user-defined altitude, is at least partially visible from the observing station, subject to the relevant line-of-sight and geometric constraints. To determine the instantaneous position of the shadow boundary, the umbra is modeled using the Spherical Earth Conical Shadow Model (SECSM)[14,15] , which represents the Earth's shadow as a right circular cone extending into space, as depicted in Figure 2. This conical representation permits real-time computation of the shadow boundary coordinates, from which the appropriate sensor pointing sequence is derived and continuously updated to maintain optimal phase angles for measurement.

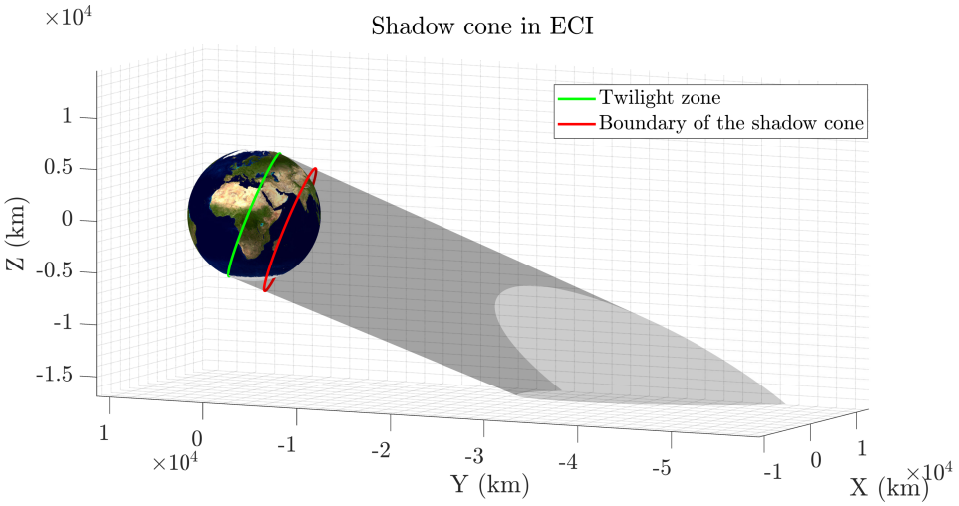

Figure 2: Earth's shadow cone in Earth-Centered Inertial (ECI) J2000 frame. The green curve marks the terminator-the boundary between Earth's day side and night side-while the red curves trace the edges of the shadow cone at an altitude of 1,000 km.

However, constructing a scanning sequence that follows the shadow cone boundary demands continuous updating, since Earth's rotation causes the cone to shift rapidly and may result in inadvertent pointing into shaded regions. For this reason, a continuous dynamical adaption to the real-time topocentric position of the border is necessary, and this is obtained by computing again the new edge after one full scansion of the shadow cone. Because the duration of

DOI: 10.13009/EUCASS2025-466

a complete scan is short relative to the rate at which the shadow cone drifts, the previously calculated pointing directions remain illuminated throughout the single full scan. This approach thus strikes an effective balance between computational efficiency in performing boundary calculations at discrete intervals and the need for a near-continuous, dynamically accurate pointing sequence.
Furthermore, determining the optimal pointing sequence is complicated by the fact that the Sun's shadow cone boundary changes shape within the topocentric reference frame. As a result, the illuminated portion of this boundary does not necessarily correspond to the exterior region of the curve projected onto the topocentric sphere. Specifically, the intersection between the circular cross-section of the shadow cone and the hemispherical representation of the sky can alter the resulting dark region. As a result, the observation strategy may, in certain cases, require redirecting the sensor toward the inner segment of the curve that delineates the sunlit portion of the sky. Figure 3 presents a single complete scan of the visible portion of the shadow cone, depicted in both planar and three-dimensional views.

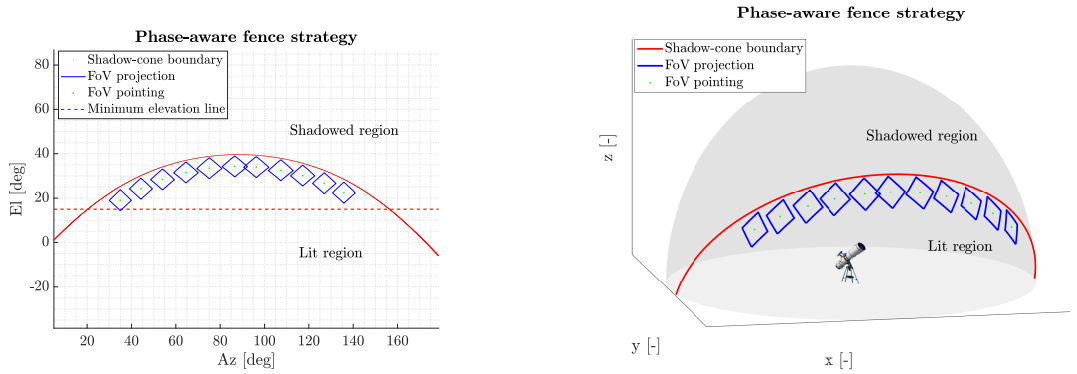

(a) 2D topocentric representation.

(b) 3D topocentric representation.

Figure 3: Representation of one full phase-aware fence scansion of the shadow cone boundary in the 2D topocentric reference frame (a) and in the 3D topocentric reference frame (b).

On the other hand, the equatorial fence strategy is delivered whenever the observing station is in local darkness and the Earth's shadow cone is not visible, thereby providing complementary coverage across orbital regimes. In this mode, the Earth's equatorial plane is projected at a user-defined altitude, typically between 2,000 km and 35,786 km to encompass both MEO and GEO populations[12] , and is scanned in a serpentine pattern (Figure 4) to capture objects as they cross the equatorial plane. Since the equatorial projection exhibits minimal apparent motion during a single scan, the initial pointing sequence remains valid throughout. However, the projection is recalculated after each complete scan to maintain pointing accuracy and enhance revisit rates.

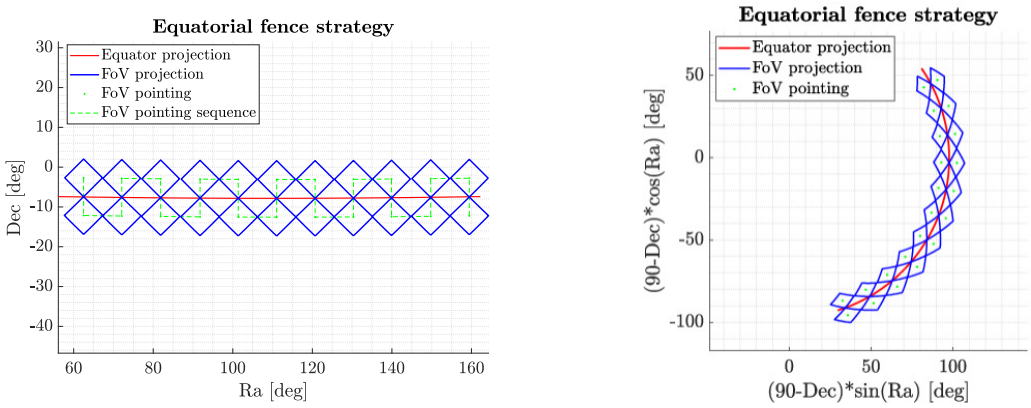

(a) Equatorial representation.

(b) Polar projection representation.

Figure 4: Representation of one full equatorial fence scansion of the equator projection in the equatorial coordinate system (Right Ascension and Declination) centered in the station (a) and the related polar projection (b).

In both strategies, repeated acquisitions of the same Field-of-View (FoV) can be performed to enhance the quality of astrometric reduction. The final observation strategy parameters employed in this work are summarized in Table 1.

DOI: 10.13009/EUCASS2025-466

Table 1: Observation strategy settings employed within this work.

Parameter [u.o.m.]	**Phase-aware fence**	**Equatorial fence**
Exposure time [s]	1.0	10.0
Readout time [s]	4.0	4.0
Projection altitude [km]	1,000	28,000
Number of acquisitions per FoV [-]	3	3

This strategy has been specifically developed for optical sensors, which alone enable comprehensive coverage across diverse orbital regimes.

3.2 Track-to-track association and IOD

The Two-Body Integrals (TBI)[7–9] method aims to provide an initial estimate of the orbit associated with a pair of observational tracks and to assess the likelihood that they originate from the same object.
This method belongs to the class of IOD techniques that require only two sets of attributables to solve the problem. An attributable is a vector containing the observational data:

$$\mathcal{A} = (\alpha, \delta, \dot{\alpha}, \dot{\delta}) \in [-\pi, \pi) \times (-\pi/2, \pi/2) \times \mathbb{R}^2 \ ,$$

representing the angular position and velocity of the body at the average time $\bar{t}$ of observations in the selected reference frame. Given the attributable $\mathcal{A}$, that is a four-dimensional vector, to compute a full orbit, formed by six parameters, the computation of two further at the same time instant, is needed.[8] The unknown quantities are the ranges (ρ) and range rates ($\dot{\rho}$) corresponding to the two attributables. However, by exploiting the problem structure, the number of unknowns can be reduced to only the two ranges, with the corresponding range rates expressed as functions of these.
The TBI method assumes an ideal and unperturbed dynamical model. Under this assumption, the conserved quantities of the two-body problem namely, the angular momentum vector $\mathbf{h}$, the Laplace-Lenz vector $\mathbf{L}$, and the orbital energy E, remain constant. The residuals of these quantities are exploited to build up a nonlinear system of equations with the two range values as unknowns as done in.[7] Solving this system by setting the residuals to zero yields the values of ρ_1 and ρ_2, from which the corresponding $\dot{\rho}_1$ and $\dot{\rho}_2$ can be computed.
An initial guess for the values of ρ_1 and ρ_2 is required to initialize the solver. This estimate is obtained through a preliminary application of Gauss' method, which uses the full track data along with the associated observation epochs.

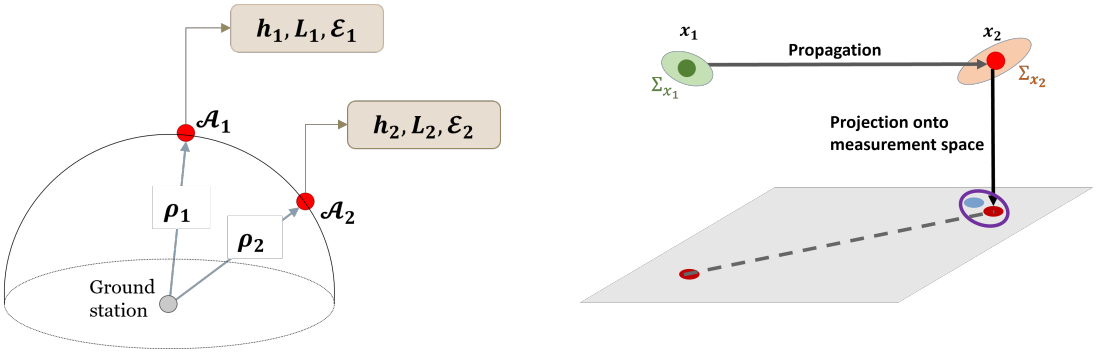

Figure 5: Visual representation of the TBI method (a) and the measurement correlation (b) steps.

Once the complete set of range and range-rate values is determined (ρ_1, ρ_2, $\dot{\rho}_1$, $\dot{\rho}_2$), the corresponding orbital states $\mathbf{x_1}(t_1)$ and $\mathbf{x_2}(t_2)$ can be reconstructed by converting from spherical to Cartesian coordinates. The state $\mathbf{x_1}(t_1)$ is then propagated using Keplerian dynamics to the epoch of the first observation, resulting in the orbit estimate $\mathbf{x}_{\text{IOD}}$.
This output can be deterministic if no measurement uncertainty (mean and covariance) is provided, or stochastic. In the stochastic case, when the mean and covariance of the observations are available, the entire process is embedded within an Unscented Transformation (UT), yielding the mean and covariance of $\mathbf{x}_{\text{IOD}}$.

DOI: 10.13009/EUCASS2025-466

For the purpose of correlation assessment, an initial check is performed on the covariance of $\mathbf{x}_{\text{IOD}}$ against predefined thresholds. Subsequently, the correlation hypothesis is verified by means Squared Mahalanobis Distance (SMD) based metric. The estimated state distribution is propagated to the epochs of the observations within both tracks and projected onto the measurement space and compared against the actual measurements distribution via SMD. The SMD can be directly compared with a n-variable $\chi^2_{n,c}$ distribution quantifying its distance through a predefined confidence level c (related to a 3-σ factor distance from its mean), leading to the definition of the correlation index $corr_{idx} = \text{SMD}(x)/\chi^2_{n,c}$. Correlation is confirmed if $corr_{idx}$ falls below the threshold of 1.

4. Simulations and results

This Section presents the simulation setup and corresponding results obtained using the SΞNSIT framework. First, Subsection 4.1 describes the population of RSOs selected from the Space-Track catalog[1] , including the altitude-based classification into HLEO, MEO, and GEO regimes. Next, Subsection 4.2 details the simulated ground-based sensor parameters, such as geographic location, Field-of-View (FoV), and visibility constraints, as well as the observation strategy settings. Subsection 4.3 reports the overall cataloging performance: Subsection 4.3.1 quantifies the number of detected passes per regime over one- and three-month intervals, highlighting the influence of orbital characteristics on detection efficiency; Subsection 4.3.2 will evaluate the track-to-track association performance of the proposed pipeline.

4.1 Population

The analysis draws on the Space-Track catalog[1]-a publicly accessible subset of the U.S. Space Surveillance Network maintained by the 18^{th} Space Defense Squadron of USSPACECOM-with all objects that lack a valid Radar Cross Section (RCS) category, have already decayed (re-entered Earth's atmosphere), or possess erroneous or incomplete Two-Line Element (TLE) data removed before further processing.
The final dataset contains 3,119 objects spanning three orbital regimes-HLEO, MEO, and GEO-as illustrated in Figure 6 and Figure 7. Each regime is defined by a specific altitude range; Table 2 summarizes their respective altitude limits and population counts.

Table 2: Orbital regimes defined by altitude ranges and corresponding object counts after filtering.

Orbital Regime	**Minimum Altitude [km]**	**Maximum Altitude [km]**	**Number of Objects**
HLEO	1,000	2,000	1,701
MEO	2,000	33,786	259
GEO	33,786	37,786	1,159
Total	-	-	3,119

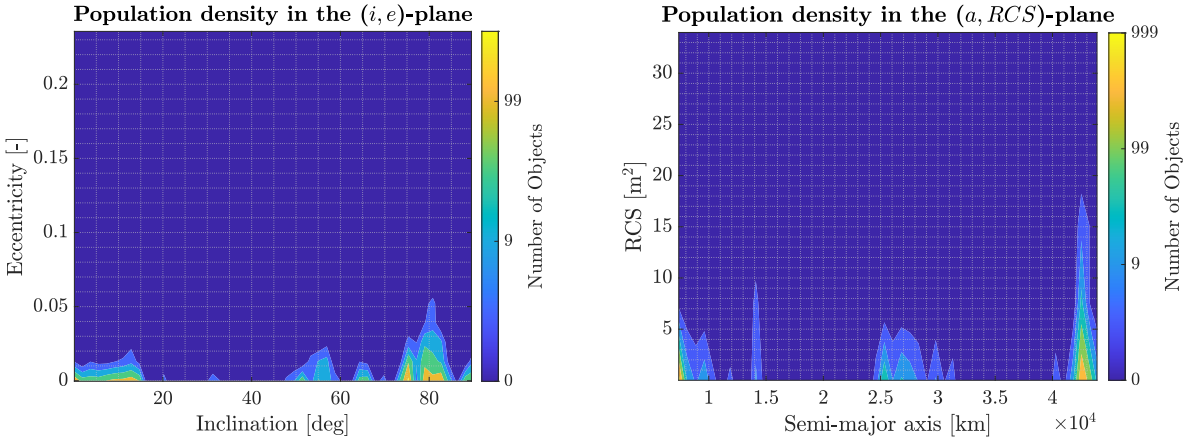

(a) Inclination-eccentricity plane representation.

(b) Semi-major axis-RCS plane representation.

Figure 6: Density distribution of simulated objects as a function of orbital and physical parameters. (a) Variation of density with orbital eccentricity (e) and inclination (i). (b) Variation of density with semi-major axis (a) and RCS.

DOI: 10.13009/EUCASS2025-466

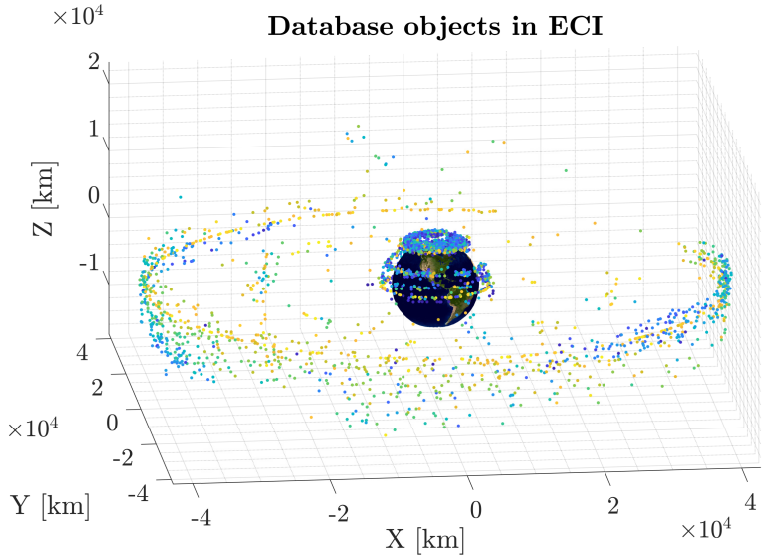

Figure 7: Distribution of the simulated HLEO, MEO, and GEO objects (sourced from Space-Track[1]) plotted in the ECI J2000 reference frame.

4.2 Sensor Definition

The sensor used in the simulation is located in Italy at latitude 39.66140°, longitude 9.43250°, and altitude 0.638 km, as shown in Figure 8. It features a square FoV of angular size $6.7° \times 6.7°$, which is rotated by 45° around its boresight axis.
The visibility constraints applied during the simulation include a minimum target elevation of 15° and a maximum Sun elevation of $-10°$. Additionally, any observation pass with an SNR below 5 was discarded. The SNR was computed using the internal photometric model implemented in the SΞNSIT framework.
To define the observation strategy within SΞNSIT, additional optional parameters must be specified. These parameters-which vary depending on the selected strategy (e.g., phase-aware fence, equatorial fence, or their combination)-are summarized in Table 1.

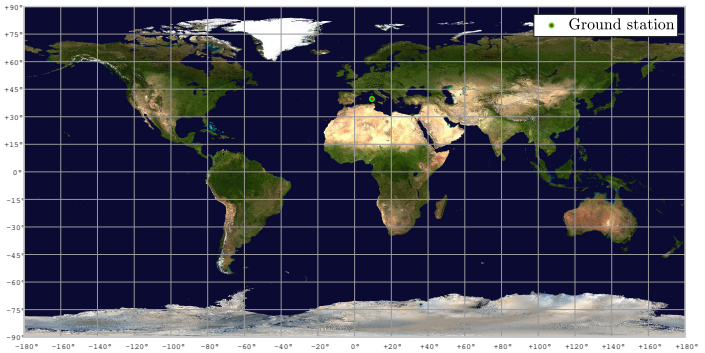

(a) Global view of the Earth's planisphere illustrating the simulated ground station location (red and green dot) relative to latitude and longitude lines.

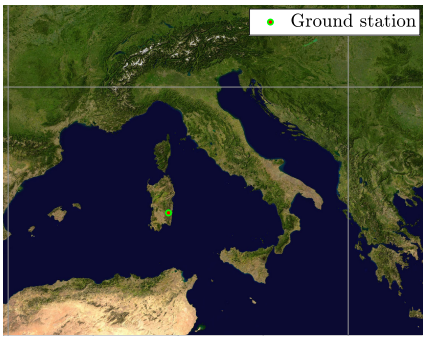

(b) Zoomed-in detail around the ground station position.

Figure 8: Simulated ground station placement on a planisphere. (a) Global map of Earth (Mercator projection) displaying the ground station marked by a red and green dot. (b) Magnified view of the immediate region surrounding the station.

DOI: 10.13009/EUCASS2025-466

4.3 Results

4.3.1 Detected Passes

To assess the validity of the proposed observation strategy, two separate simulations were performed: a one-month observation campaign and a three-month campaign, each beginning on January 1st, 2024. The efficiency of the strategy in covering the entire Field of Regard (FoR) was evaluated by comparing the number of detected objects with the total number of objects that entered the sensor FoR at least once during the respective time window. Table 3 presents the detection performance for each orbital regime, HLEO, MEO, and GEO, as well as the overall performance.

Table 3: Detection performance over one-month and three-month observation windows. Each value represents the ratio of detected objects to the total number of objects that entered the FoR, followed by the corresponding percentage.

Time Window	HLEO	MEO	GEO	Total
1 month	1,139/1428 → 79.76%	237/256 → 92.58%	581/676 → 85.95%	1,957/2,360 → 82.92%
3 months	1,565/1,701 → 92.00%	253/258 → 98.06%	770/816 → 94.36	2,588/2,775 → 93.26%

As shown in the results, the detection performance is lower for HLEO objects. This is primarily due to their higher angular velocities, which make them more difficult to capture during the FoR scanning process defined by the observation strategy.
It is important to note that multiple detected passes are typically required to maintain an object in the catalog. Here, a pass refers to a single transit of an object through the FoR; however, an object can be observed multiple times during the same pass. Figure 9 illustrates that the number of detected passes per object is generally high, especially in the three-month simulation, indicating that the proposed strategy is effective not only in detecting objects but also in enabling multiple re-observations.

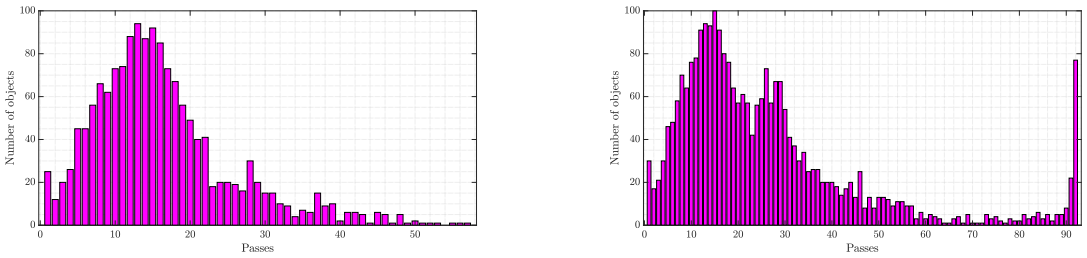

(a) 1-month simulation. (b) 3-months simulation.

Figure 9: Distribution of the number of detected passes per object.

Additionally, the effectiveness of the phase-aware fence in conjunction with the optical telescope for detecting small objects in the HLEO population is illustrated in Figure 10. These images display a coverage histogram with the proportion of objects detected across the entire population as a function of their RCS.

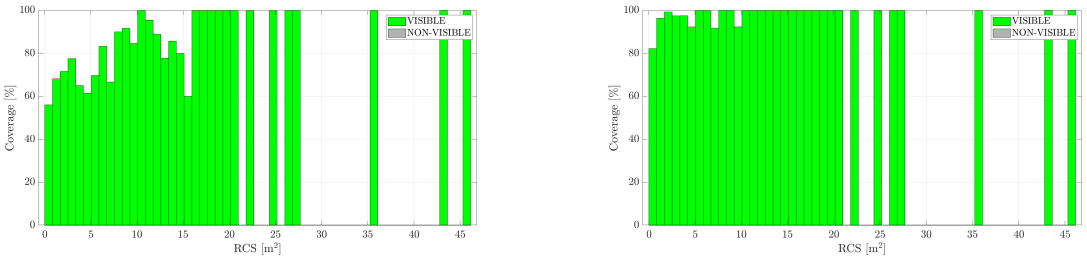

(a) 1-month simulation. (b) 3-months simulation.

Figure 10: RCS-based coverage histogram after one and three months of simulation.

In these last plots, a gray bar would indicate that objects fall within a specific RCS range. Notably, no gray bars are present, indicating that the observation strategy successfully detects objects across the full range of RCS values.

DOI: 10.13009/EUCASS2025-466

It is also important to note that the histogram considers the entire population, not just objects passing through the sensor FoR. As a result, overall performance is expected to further improve with the deployment of a distributed sensor network instead of a single sensor installation.

4.3.2 Track-to-track and cataloging

This section presents the results of the simulation previously described, for the three orbital regimes analyzed. For each regime, an all-vs-all analysis was performed using tracks associated with 100 representative objects from the respective orbital population. Only track pairs with a time separation of at most 24 hours were considered for this analysis from the one month simulation passes list, computed in Subsection 4.3.1.
The total number of track pairs examined in each case was: 74,876 GEO pairs, 181,192 MEO pairs and 29,372 HLEO pairs. A statistical analysis was conducted on the outputs in terms of:

- **True Positive (TP)**: number of correct associations ($corr_{idx} \leq 1$), with respect to the total number of track pairs that should have been correctly associated (percentage).
- **False Negative (FN)**: number of failed associations ($corr_{idx} > 1$) that should have returned a positive result, with respect to the total number of track pairs that should have been correctly associated (percentage).
- **True Negative (TN)**: Number of failed associations ($corr_{idx} > 1$) because they did not belong to the analyzed objects, with respect to the total number of examined track pairs (percentage).
- **False Positive (FP)**: number of positive associations ($corr_{idx} \leq 1$), wrongly matched because they belonged to different objects, with respect to the total number of examined track pairs (percentage).
- **Failed**: number of failed association processes due to the non-convergence of the IOD method, occurring in the HLEO cases (percentage).

The reported statistics were derived using a threshold for a correct association between tracks defined as a correlation index value $corr_{idx} \leq 1$. This choice represents a conservative approach by applying the strictest condition, in order to limit the number of FP as much as possible. In the GEO and MEO regimes, the percentage of TP is relatively high;

Orbital Regime	TP	FN	TN	FP	Failed
GEO	79.5419 %	20.4581 %	85.0154 %	13.5216 %	0 %
MEO	85.6722 %	14.3278 %	99.7416 %	0.2584 %	0 %
HLEO	30.6723 %	68.4874 %	99.9944 %	0.0056%	0.8403 %

Table 4: Correlation outcomes statistics for a dataset of GEO,MEO and HLEO objects having a time span between tracks of maximum 1 day.

however, both cases exhibit a notable proportion of FN. The highest FP rate is observed in the GEO regime. As shown in Figure 11(a), these false associations are predominantly concentrated around a time separation of 24 hours. This aligns with the orbital period of GEO objects, making it more likely to mistakenly associate measurements belonging to this regime. Figures 11(a) and 11(b) illustrate a clear inverse trend between TP and FP: TP values are concentrated at low Δt (within a few hours), whereas FP rates tend to increase with larger time separations. Since in the GEO and MEO regimes, short-term dynamical stability favors correct associations for small Δt, while the accumulation of propagation errors and the reduced orbital discriminability over longer time spans lead to incorrect associations. This results in an inversely proportional trend between TP and FP as a function of the time interval between tracks.
In contrast, the HLEO case exhibits a generally low TP rate throughout the observation window, with successful associations concentrated mainly at very short Δt intervals. This behavior can be attributed to the higher sensitivity of the HLEO regime to orbital perturbations, which evolve more rapidly than in GEO and MEO. As shown in Figure 11(c), the TP rate drops sharply as the time difference increases. However, the FP rate is significantly lower than in the other two regimes.
A distinctive feature of the HLEO analysis is the presence of a substantial fraction of failed association processes, reported in the Failed column of Table 10. These failures are primarily due to the inability of the Two-Body Integral method to converge to physically consistent solutions under the conditions typical of the HLEO regime. Additionally, Figure 11(b) confirms that TP associations are clustered at low Δt, while the low FP associations tend to occur near the 24-hour threshold.

DOI: 10.13009/EUCASS2025-466

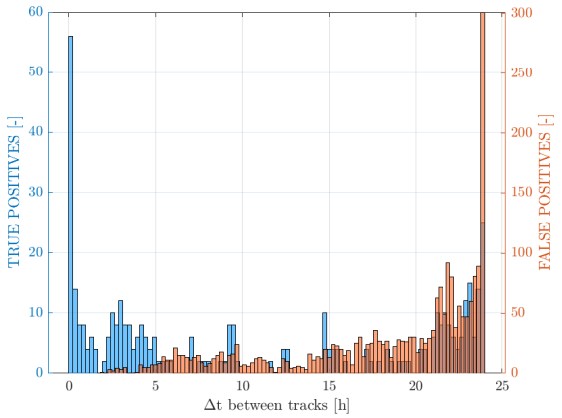

(a) GEO TP and FP (1 day).

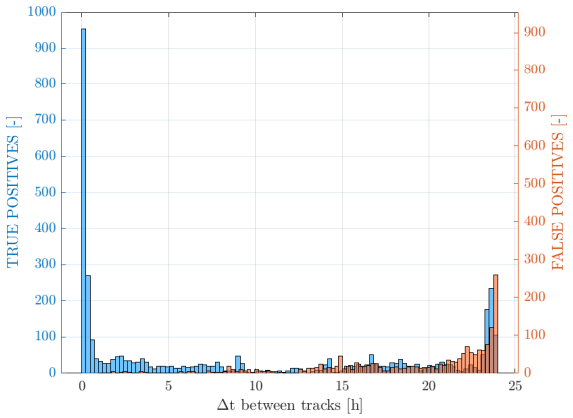

(b) MEO TP and FP (1 day).

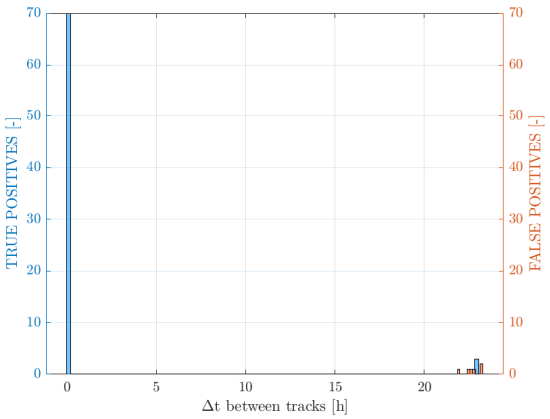

(c) HLEO TP and FP (1 day).

Figure 11: Distribution of True Positive and False Negative track-to-track correlation results for 100 GEO objects (a), 100 MEO objects (b) and 100 HLEO objects (c) considering a maximum of 1 day time gap between tracks.

5. Conclusions

Space Surveillance and Tracking remains a critical component of space operations, supporting collision avoidance, space object monitoring, and the long-term sustainability of orbital environments. This study presents and evaluates an advanced composite observation strategy, integrating a phase-aware fence for HLEO targets and an equatorial fence for MEO-GEO populations, implemented within the enhanced SΞNSIT simulation framework. Nightly campaign simulations demonstrate that this dual-mode approach effectively covers multiple orbital regimes, achieving detection rates of up to 92% for HLEO, 98% for MEO, and 94% for GEO objects over a three-month period. Additionally, the strategy ensures high revisit frequency, with most objects observed multiple times within the time window, thereby enhancing catalog stability. A dedicated track-to-track association pipeline, leveraging the Two-Body Integrals method for initial orbit determination and a χ^2-based validation using the Squared Mahalanobis Distance, has been shown to produce robust correlation outcomes across orbital regimes. True positive association rates exceeded 85% in both MEO and GEO, with false positive rates confined below 1%, while HLEO associations achieved up to 31% true positives for short-time separations and maintained a low false positive incidence. The inclusion of uncertainty propagation via an Unscented Transformation further supports adaptive thresholding, enhancing confidence in catalog entries and minimizing spurious correlations.

Regarding future developments, the methodology presented here can be further evaluated by incorporating objects with smaller RCS into the simulated population, in order to assess detection limits under more challenging photometric conditions. Furthermore, simulating a geographically distributed network of optical sensors would extend the applicability of the proposed strategies, mitigating coverage gaps and better representing the capabilities of a global surveillance architecture. Moreover, refining the initial orbit determination algorithms-potentially through the integration of pertur-

DOI: 10.13009/EUCASS2025-466

bation models or hybrid IOD techniques-and optimizing correlation thresholds for specific orbital regimes will serve to enhance both detection fidelity and catalog maintenance. These advancements will contribute to a more resilient and accurate SST architecture, essential for safeguarding both current and future space activities.

6. Aknowledgments

The authors gratefully acknowledge Leonardo Company for its invaluable collaboration in the development and realization of the C2-SSA Project. This work was supported by the agreement no. 2023-37-HH.0, "Attivita' tecnico-scientifiche di supporto a C-SSA/ISOC e simulazione di architetture di sensori per SST" between the Italian Space Agency (ASI) and Politecnico di Milano (PoliMi), under which Mr. Mignocchi's research was funded. The contributions of Mr. Rizzuto and Ms. De Riz have been made possible thanks to funding from the European Union - NextGenerationEU, under Mission 4, Component 1 (CUP: D43C23002190008), whose support is gratefully acknowledged.

References

[1] 18^{th} Space Defense Squadron. Space-mission-related data from Space-Track.org. `https://www.space-track.org/`, 2025. Retrieved April 15, 2025.

[2] C. Acton, N. Bachman, B. Semenov, and E. Wright. SPICE tools supporting planetary remote sensing. *The International Archives of the Photogrammetry, Remote Sensing and Spatial Information Sciences*, 41:357–359, 2016.

[3] C. Acton, N. Bachman, B. Semenov, and E. Wright. A look towards the future in the handling of space science mission geometry. *Planetary and Space Science*, 150:9–12, 2018. Enabling Open and Interoperable Access to Planetary Science and Heliophysics Databases and Tools.

[4] S. Bonaccorsi, M.F. Montaruli, P. Di Lizia, M. Peroni, A. Panico, M. Rigamonti, and F. Del Prete. Conjunction analysis software suite for space surveillance and tracking. *Aerospace*, 11(2):122, 2024.

[5] P. Faucher, R. Peldszus, and A. Gravier. Operational space surveillance and tracking in europe. *Journal of Space Safety Engineering*, 7(3):420–425, 2020.

[6] T. Flohrer, H. Krag, H. Klinkrad, and T. Schildknecht. Feasibility of performing space surveillance tasks with a proposed space-based optical architecture. *Advances in space research*, 47(6):1029–1042, 2011.

[7] G.F. Gronchi, G. Bau, and S. Maro. Orbit determination with the two-body integrals: III. *Celestial Mechanics and Dynamical Astronomy*, 123:105–122, 2015.

[8] G.F. Gronchi, L. Dimare, and A. Milani. Orbit determination with the two-body integrals. *Celestial Mechanics and Dynamical Astronomy*, 107(3):299–318, 2010.

[9] G.F. Gronchi, D. Farnocchia, and L. Dimare. Orbit determination with the two-body integrals. II. *Celestial Mechanics and Dynamical Astronomy*, 110(3):257–270, 2011.

[10] B.D Little and C. Frueh. Space situational awareness sensor tasking: comparison of machine learning with classical optimization methods. *Journal of Guidance, Control, and Dynamics*, 43(2):262–273, 2020.

[11] G. Purpura, A. De Vittori, R. Cipollone, P. Di Lizia, M. Massari, C. Colombo, A. Di Cecco, and L. Salotti. SΞNSIT: a software suite for observation scheduling and performance assessment of sst sensor networks. In *Proceedings of the 72nd International Astronautical Congress*, pages 1–13, Dubai, United Arab Emirates, October 2021. International Astronautical Federation.

[12] T. Qiu, Y. Wang, J. Hong, K. Xing, S. Du, and J. Mu. An in-orbit measurement method for elevation antenna pattern of meo synthetic aperture radar based on nano calibration satellite. *Remote Sensing*, 14(3):741, 2022.

[13] J. Rowland, D. McKnight, B.P. Pino, B. Reihs, and M.A. Stevenson. A worldwide network of radars for space domain awareness in low earth orbit. In *Advanced Maui Optical and Space Surveillance Technologies Conference (AMOS)*, 2021.

DOI: 10.13009/EUCASS2025-466

[14] V.K. Srivastava, A. Ashutosh, M.V. Roopa, B.N. Ramakrishna, M. Pitchaimani, and B.S. Chandrasekhar. Spherical and oblate earth conical shadow models for leo satellites: Applications and comparisons with real time data and stk to irs satellites. *Aerospace Science and Technology*, 33(1):135–144, 2014.

[15] R. Zhang, R. Tu, P. Zhang, J. Liu, and X. Lu. Study of satellite shadow function model considering the overlapping parts of earth shadow and moon shadow and its application to gps satellite orbit determination. *Advances in Space Research*, 63(9):2912–2929, 2019.